Energy & Environmental Science

Accepted Manuscript

ROYAL SOCIETY OF CHEMISTRY

www.rsc.org/ees

Broader context

High-performance SnTe materials are promising for thermoelectric power generation, e.g., by harvesting widespread waste heat. However, compared with its Pb analogue , the key limitations of SnTe are its intrinsically super-high carrier concentration, low Seebeck coefficient and high thermal conductivity. Generally, the overall thermoelectric properties can be enhanced through: (1) enhancing the electrical transport *via* carrier concentration tuning and band structure engineering (e.g. resonant states and band convergence); (2) lowering the lattice thermal transport by hierarchical architecturing; (3) suppressing the bipolar effect *via* enlarging the band gap. In the present work, we introduce a single element Mn in SnTe. Mn exhibits extremely high solid solution in SnTe (>13%), and thus it can strikingly modify the band structure and microstructure of SnTe. Heavy Mn alloying can significantly improve the electrical and thermal transport properties of SnTe *via* band structure modifying, multiple phonon scattering and bipolar thermal conductivity suppressing. The integration of these effects yields a high *ZT* of 1.3 at 900 K and high average *ZT* value of ~0.5 (from 300 K to 900 K).

Synergistically optimized electrical and thermal transport properties in SnTe *via* alloying high-solubility MnTe

Haijun Wu,[1,2,#] Cheng Chang,[1] Dan Feng,[2] Yu Xiao,[1] Xiao Zhang,[1] Yanling Pei,[1] Lei Zheng,[1] Di Wu,[2] Shengkai Gong,[1] Yue Chen,[3] Jiaqing He,[2*] Mercouri G. Kanatzidis,[4*] Li-Dong Zhao[1*]

[1]School of Materials Science and Engineering, Beihang University, Beijing, 100191, China

[2]Department of Physics, South University of Science and Technology of China, Shenzhen, 518055, China

[3]Department of Mechanical Engineering, The University of Hong Kong, Pokfulam Road, Hong Kong SAR China

[4]Department of Chemistry, Northwestern University, Evanston, Illinois 60208, United States

[#]Present addresses: Department of Materials Science and Engineering, National University of Singapore, 7 Engineering Drive 1, Singapore 117574, Singapore.

*Corresponding authors: zhaolidong@buaa.edu.cn; he.jq@sustc.edu.cn; m-kanatzidis@northwestern.edu

Abstract

Lead chalcogenides are the most efficient thermoelectric materials. In comparison, SnTe, a lead-free analogue of PbTe, exhibits inferior thermoelectric performance due to low Seebeck coefficient and high thermal conductivity. In this report, we show that we can synergistically optimize electrical and thermal transport properties of SnTe *via* alloying Mn. We report that the introduction of Mn (0-50%) induces multiple effects on band structure and microstructure of SnTe: for the former, it can tune the Fermi level and promote the convergence of the two valence bands, concurrently enhancing the Seebeck coefficient; for the latter, it can profoundly modify microstructure into an all-scale hierarchical architecture (including nanoscale precipitates/MnTe laminates, stacking faults, layered structure, and atomic-scale point defects, *etc*.) to scatter phonons with broad range of mean free paths, strongly reducing the lattice thermal conductivity. Meanwhile, most significantly, the Mn alloying enlarges the energy gap of conduction band (*C* band) and light valence band (*L* band), thereby suppresses the bipolar thermal conductivity through increasing band gap. The integration of these effects yields a high *ZT* of 1.3 at 900 K for 17% Mn alloyed SnTe.

1. Introduction

Thermoelectric materials enable the direct inter-conversion between electrical energy and thermal energy, and are regarded as a promising technology for energy saving and generation, e.g., harvesting widespread waste heat. Currently, some of the most advanced thermoelectric materials are lead chalcogenides (PbQ, Q = Te, Se and S) and their solid solutions. [1-7] SnTe, as a lead-free analogue of PbTe, is considered as a possible substitute of PbTe for thermoelectric power generation, since it possesses similar crystal structure and electronic band structure with PbTe.[8, 9] However, SnTe exhibits much lower thermoelectric performance than PbTe because of the following aspects: (1) too high hole density (>10^{21} cm^{-3}) due to the "intrinsically" large number of Sn vacancies; (2) too small band gap (0.18 eV) and too large energy separation (0.35 eV) between the light- and heavy-hole bands with respect to PbTe (0.30 eV and 0.17 eV, respectively), which induce significant bipolar conduction; (3) too high lattice thermal conductivity (~3.5 $Wm^{-1}K^{-1}$ for SnTe vs. 1.5 $Wm^{-1}K^{-1}$ for PbTe at 300 K).[10-15] The first two properties concurrently result in lower Seebeck coefficient, especially at elevated temperatures, compared with PbTe. Therefore both electrical and thermal transport properties of SnTe need to be optimized.

The overall performance of thermoelectric materials is governed by the dimensionless figure of merit, $ZT=(S^2\sigma/\kappa)T$, where S and σ are the Seebeck coefficient and electrical conductivity, which constitute the electrical transport properties (power factor); κ is thermal conductivity.[16-20] In PbQ systems, persistent efforts succeeded to enhance ZT through enhancing the electrical transport (α and σ) *via* carrier concentration tuning[21, 22] and/or band structure engineering (e.g. resonant states and band convergence),[2, 4, 5] and also through lowering the thermal transport (κ) by hierarchical architecturing.[3-5] Considering the similarity between SnTe and PbTe in rock-salt structure and valence bands features, researchers have employed similar concepts (as in PbTe) and achieved a serial of successes in SnTe systems.[10-15] For example, In dopants can modify the band structure of SnTe by creating resonant levels in the valence bands, thus considerably increasing the Seebeck coefficient.[10] On the other hand Cd, Hg, and Mg alloying can enhance the Seebeck coefficient through the

convergence of the two valence bands.[11, 14, 15] When CdS, HgTe, ZnS nanoprecipitates are introduced as second phases in the system, they can strongly scatter heat carrying phonons to significantly reduce lattice thermal conductivity.[13]

Very recently, Tan reported that Mn alloying SnTe (0-15%) could also enhance its overall thermoelectric properties, like Cd, Hg and Mg.[23] However, we noticed that Mn exhibits an extremely high solid solution in SnTe (>13%), much more ubiquitous hierarchical architectures for scattering phonons are expected when the solubility limit of Mn in SnTe is exceeded. In this study, we introduce a significantly wider fraction of Mn into SnTe (0-50%) and investigated its broad effects on the microstructure of SnTe. Heavily MnTe alloying can significantly improve the electrical and thermal transport properties of SnTe *via* band structure engineering, multiple phonon scattering and bipolar thermal conductivity suppressing. Here, we present more systemically investigations on Pisarenko relationships, and analyze the significant effects on band structures after introducing Mn in SnTe, by the use of first-principles density functional theory (DFT) calculations. A high *ZT* of 1.3 is achieved at 900 K for SnTe alloyed with 17% MnTe. We attribute the high thermoelectric performance to a synergistic combination of enhanced power factor, reduction of the lattice thermal conductivity and simultaneous suppression of bipolar thermal conductivity. The MnTe inclusion in SnTe accomplishes three functions: the Mn alloying within the solubility limit (estimated around 13%) in SnTe modifies the valence band structure by pushing the two valence bands (*L* and *Σ* bands) closer in energy, thereby facilitating multi-band conduction. When the solubility limit of Mn is exceeded, ubiquitous endotaxial nanostructures form, which when coupled with mesoscale microstructuring result in a very low (lattice) thermal conductivity through all-scale phonon scattering. Meanwhile, most significantly, the Mn alloying enlarges the energy gap of conduction band (*C* band) and light valence band (*L* band), and suppresses the bipolar thermal conductivity.

2. Experimental procedures

2.1. Raw materials

Sn chunk (99.9999%, American Elements, US), Mn shots (99.98%, Sigma-Aldrich, US) and Te shot (99.999%, Sigma-Aldrich, US)

2.2. Synthesis

A series of $Sn_{1-x}Mn_xTe$ (x=0, 1%, 3%, 5%, 7%, 9%, 11%, 13%, 15%, 17%, 19%, 20%, 25% and 50%, in mole ratio) were synthesized by mixing appreciated ratios of high purity starting materials in Ø ~ 8 mm silica tubes in an N_2-filled glove box. The tubes were then evacuated to a pressure of ~10^{-4} torr, flame-sealed, slowly heated to 723 K in 12 h, then to 1423 K in 7 h, soaked at this temperature for 6h and subsequently air quenched to room temperature. The obtained ingots were crushed into fine powders <5 mm^3 and further ground with mortar and pestle. The selected fine powders were densified using spark plasma sintering (SPS-211Lx, Dr. Sinter) at 823 K for 10 min with a 60 MPa uniaxial pressure, highly dense samples can achieve >97% of theoretical density.

2.3. Electron Microscopy and X-ray Diffraction

(Scanning) transmission electron microscopy (S/TEM) and energy dispersive spectroscopy (EDS) experiments investigations were carried out using a Tecnai F30 microscope operated at 200 kV. The thin TEM specimens were prepared by conventional methods, including cutting, grinding, dimpling, tripod, with minimal duration of Ar-ion milling with a liquid nitrogen cooling stage.

Samples pulverized with an agate mortar were used for powder X-ray diffraction (XRD). The powder diffraction patterns were obtained with Cu K_α (λ=1.5418Å) radiation in a reflection geometry on an Inel diffractometer operating at 40 kV and 20 mA and equipped with a position-sensitive detector. The phases in the samples were analyzed with JADE 5.0 software. The Rietveld refinements of the XRD patterns were performed using Topas 3.1 software.

2.4. Physical Characterization

Electrical Properties: The obtained SPS processed pellets were cut into bars with dimensions 12 × 3 × 3 mm^3 for simultaneous measurement of the Seebeck coefficient and electrical conductivity using an Ulvac Riko ZEM-3 instrument under a low-pressure helium atmosphere from room temperature to 900 K. The uncertainty of

the Seebeck coefficient and electrical conductivity measurements is 5%.[5]

Thermal Conductivity: Highly dense SPS processed pellets were cut and polished into a squared shape of 6 × 6 × 2 mm^3 for thermal diffusivity measurements. The samples were coated with a thin layer of graphite to minimize errors from the emissivity of the material. The total thermal conductivity was calculated from $\kappa_{tot} = D \bullet C_p \bullet d$, where the thermal diffusivity coefficient (D) was measured using the laser flash diffusivity method in a Netzsch LFA457, the specific heat capacity (C_p) was indirectly derived using a representative sample (Pyroceram 9606) in the range 300-923 K, and the density (d) was determined using the dimensions and mass of the sample (>95% relative density, Table S1). The thermal diffusivity data were analyzed using a Cowan model with pulse correction. The uncertainty of the thermal conductivity is estimated to be within 8%, considering all the uncertainties from D, C_p, and d. The lattice thermal conductivity (κ_{lat}) was calculated by subtracting the electrical thermal conductivity (κ_{ele}) from κ_{tot} using a Wiedemann-Franz relationship $\kappa_{ele}=L \cdot \sigma \cdot T$, where L is Lorenz number which can be obtained by fitting the Seebeck coefficient to the reduced chemical potential.[24] The combined uncertainty for all measurements involved in the calculation of ZT is less than 20%.

Hall Measurements: Room Hall coefficients were measured on a home-built system in magnetic fields ranging from 0 to 1.25 T. High temperature Hall coefficients were measured with a homemade high temperature apparatus, which provides a working range from 300 to 923 K. The sample was mounted and protected with argon gas to avoid possible oxidation at high temperature. The Hall resistance was monitored with a Linear Research AC Resistance Bridge (LR-700), with constant magnetic fields of ±1 T applied by using an Oxford Superconducting Magnet. The effective carrier concentration (N_p) was estimated using the relationship $N_p = 1/(e \cdot R_H)$, where e is the elemental charge, and R_H is the Hall coefficient. The Hall mobility (μ_H) was calculated using the relationship $\mu_H = \sigma \cdot R_H$ with σ being the electrical conductivity obtained from ZEM-3 instrument.

2.5. Electronic structure calculations

The electronic structures are computed within density functional theory (DFT)

using the Perdew-Burke-Ernzerhof (PBE) functional[25] as implemented in the Vienna ab initio simulation package (VASP).[26, 27] A plane wave energy cutoff of 350 eV is applied, and the energy convergence criteria for charge self-consistency is 10^{-6} eV. A Monkhorst-Pack[28] k-point mesh of 4×4×4 is applied for the self-consistent calculations of the 3×3×3 supercell of rock-salt crystal structure. Two Sn atoms in the supercell are substituted with the Mn atoms to simulate a doping concentration of about 7.4%. All possible atomic configurations of the Mn-doped supercell are considered, and both ferromagnetic (FM) and antiferromagnetic (AFM) states are investigated. All the systems are fully relaxed before the band structure calculations, where the spin-orbit coupling effects are included.

3. Results and discussion

3.1. Solid solution limit of MnTe in SnTe

The powder XRD patterns of $Sn_{1-x}Mn_xTe$ (1%≤x≤50%) are shown in Figure 1(a) exhibit a single phase that can be indexed to the rock-salt SnTe (space group Fm-3m) structure type up to x=13% MnTe. The enlarged spectra for (200) Bragg peaks (Figure 1(b)) show the shifting trend of these peaks *via* rising MnTe fractions, firstly increase to 13% and then decrease. As shown in Figure 1(c), the calculated lattice parameter decreases with increasing Mn fractions (following Vegard's law type behavior, denoted by the dashed line), consistent with the smaller radius of Mn^{2+} (~0.66 Å) compared to that of Sn^{2+} (~0.93 Å). This suggests that a solid solution limit of Mn in SnTe is around 13%. When the Mn fraction is beyond 20%, a second bulk phase MnTe can be clearly observed. Here, the XRD patterns of $Sn_{0.80}Mn_{0.20}Te$ are calculated from the Rietveld refinement.[29] Figure 1(d) shows that the $Sn_{0.80}Mn_{0.20}Te$ composite consists of two phases, the major phase is $Sn_{0.865}Mn_{0.135}Te$ (90.82 wt.%) and the second is MnTe (9.18 wt.%). The Rietveld refinement results support the solubility limit of Mn in SnTe to be about 13%. Of course, as we have pointed out in previous publications,[3, 5] the real solubility limit may be lower if nanostructures are formed (see below). Nanostructures are not readily detectable by XRD, and TEM is needed to better evaluate solubility.

3.2. Electrical transport properties

The thermoelectric properties as a function of temperature are illustrated in Figure 2 for $Sn_{1-x}Mn_xTe$ with x=0-20%. The temperature dependent electrical conductivity σ and Seebeck coefficient S for $Sn_{1-x}Mn_xTe$ samples are shown in Figures 2(a) and (b), respectively. In all samples, σ decreases with increasing temperature, while S exhibits the opposite trend. Furthermore, with rising Mn fraction, the σ decreases continuously, largely because of the dramatically decreased carrier mobility, since the hole concentration is increased by Mn alloying in SnTe, Figure S1. Specifically, the room temperature σ significantly decreases from ~7643 Scm^{-1} for pure SnTe to ~2188 Scm^{-1} for x = 9%, and further down to ~1372 Scm^{-1} for x = 20%. Compared to PbTe (~ 2500 Scm^{-1} at 300 K),[3, 4] the high electrical conductivity (~ 7500 Scm^{-1} at 300 K) mainly comes from its intrinsically high hole concentration. The continuous loss of hole mobility in SnTe with increasing Mn content (Figure S1) probably results from the variety of defects caused by the Mn inclusions in SnTe, such as point defects within solid solution, Mn-rich nanoprecipitates and layered MnTe second phases (will show later) or enhanced density of states effective mass of holes due to Mn-induced valence band convergence. It is generally expected that doping and alloying will deteriorate the carrier mobility to some degree. It the present case they seem to play multiple roles in the band structure and microstructure that tend to improve than worsen the electrical and thermal transport properties, *vide infra*. It is interesting that adding Mn increases the hole concentration (Figure S1), which hints that Mn serves as an electron acceptor in SnTe, even though Mn is isovalent with Sn. Similar phenomena were also observed when Hg, Cd and Mg are alloyed in SnTe, as shown in Figure S2.

The Seebeck coefficient S as a function of Mn alloyed fraction exhibits firstly an increasing trend followed by a decreasing one. Specifically, the room temperature S significantly increases from ~ + 7.4 μVK^{-1} for pure SnTe to ~ + 62.2 μVK^{-1} for x=13% and slightly decreases to ~ + 54.5 μVK^{-1} for x=20%; at 900 K, S remarkably enhances from ~ + 155.8 μVK^{-1} for pure SnTe to ~ + 213.9 μVK^{-1} for x=9% and slightly returns to ~ +163.2 μVK^{-1} for x=20%. Figure 2(c) shows the Seebeck coefficient comparisons

of SnTe with different dopants, among which Mn-alloyed SnTe clearly shows the highest value at high temperatures, as shown in Figure 2(d).[10-14] As reported in previous work, In dopant can increase the *S* via creating resonant levels,[10] while Cd/Hg dopants seem to modify the band structure of SnTe, i.e., valence band convergence and band gap enlargement.[11, 14] However, these roles cannot be maximized in these systems, because of the more limited solid solubility (<3%) of Cd/Hg dopants compared to Mn.[10, 11, 13, 14] Because Mn possesses much higher solid solubility it can more thoroughly modify the band structure of SnTe, and thus achieve a higher *S*.

The temperature dependent power factors of the $Sn_{1-x}Mn_xTe$ samples are plotted in Figure 2(d). The power factor at room temperature has been significantly enhanced, and reaches 7.2-7.5 $\mu Wcm^{-1}K^{-2}$ for 9-19% MnTe alloyed samples. Accordingly, the power factor at 900 K was also improved from ~16.8 $\mu Wcm^{-1}K^{-2}$ to ~24 $\mu Wcm^{-1}K^{-2}$, which rivals with that of high performance PbTe-based materials.[3-5, 24]

3.3. Band structure engineering

It is interesting that the Mn alloying increases the hole concentration, but does not deteriorate *S* over the entire temperature range. In addition, Mn alloying, like Mg, Cd, and Hg, can significantly modify the band structure of SnTe, so as to enhance the Seebeck coefficients, especially at high temperatures. First, the data suggest that Mn alloying in SnTe brings the two valence bands (*L* and *Σ*) closer in energy (ΔE_V) i.e., valance band convergence, thereby facilitating charge carrier injection. Second, Mn alloying can also enlarge the band gap between conduction band (*C*) and valance band (*L* or *Σ*), and thus hinder minority carriers (electrons) to jump across the band gap to contribute *S* adversely. Furthermore, by increasing the hole concentration *via* Mn alloying, the Fermi energy level (E_F) is lowered away from the conduction band and pushed deeper into the valence band of SnTe, which could mitigate the bipolar effect, meanwhile facilitating the participation of the heavy hole band in the carrier transport.[4] All these approaches as shown in Figure 3(a) contribute a higher *S*, especially at elevated temperature.

The well-established Pisarenko relation between Seebeck coefficient *S* and carrier concentration N_P could give valuable hints on the band structure change.[30] The black solid line is the Pisarenko line based on two valence band model (VBM).[31] The room temperature *S* vs. N_P values of Mn alloyed SnTe, as well as reported SnTe alloyed by In, Cd, Mg and Hg, were plotted for comparisons. The data pointing to SnTe from both literatures[32] and the present work can well fall on the Pisarenko line, suggesting the validity of the two valence band model in SnTe (as in PbTe). Bi/Cu-doped SnTe were reported as simple dopant in SnTe, but negligibly effect on band structure.[32] In comparison, those Mn-alloyed samples have much higher Seebeck coefficients lying above the Pisarenko line, indicative of a modified band structure, e.g., consistent with valence band convergence. To further validate the effect of Mn alloying on the band structure, the valence band convergence needs be considered within a two-band model, where each valence band is treated as parabolic. The Seebeck coefficient as the result of two types of charge carriers can be written as:

$$S = \frac{\sigma_{lh} \cdot S_{lh} + \sigma_{hh} \cdot S_{hh}}{\sigma_{lh} + \sigma_{hh}} = \frac{p_{lh}\mu_{lh}S_{lh} + p_{lh}\mu_{lh}S_{lh}}{p_{lh}\mu_{lh} + p_{lh}\mu_{lh}} \quad (1)$$

where subscripts *lh* hand *hh* denote the contributions from light-hole band and heavy-hole band separately. In the case of single parabolic band, carrier concentration and Seebeck coefficient can be correlated as follows:[33]

$$S = \pm\frac{k_B}{e}\left(\frac{(r+5/2)F_{r+2/3}(\xi)}{(r+3/2)F_{r+1/2}(\xi)} - \xi\right) \quad (2)$$

$$p = 4\pi\left(\frac{2m_d^* k_B T}{h^2}\right)^{3/2} F_{1/2}(\xi) \quad (3)$$

where Fermi integral:

$$F_n(\xi) = \int_0^\infty \frac{x^n}{1+e^{x-\xi}}dx \quad (4)$$

Scattering factor r is set to be -1/2 assuming acoustic scattering dominates. The parameter ξ is the reduced Fermi level of each band, effective mass of each band are taken from previous literature.[34] Note that the conservation of carrier concentration requires $p_{hl}+p_{hh}=N_p$, the energy offset ΔE_V between the two valence bands gives

$\xi_{hh}=\xi_{lh}-\Delta E_v/k_BT$, and that the carrier mobility μ is inversely proportional to band effective mass. Consequently, one can obtain the combined Seebeck coefficient versus carrier concentration N_p at a given temperature. We performed room temperature calculations of S vs. N_p with varying valence band offset ΔE_v, and found the experimental values are consistent with the presumption that Mn alloying results in reduced band offset between the light-hole and heavy-hole bands, i.e., ΔE_V is converged from 0.35 eV for SnTe to ~ 0.3 eV for x=$Mn_{0.01}Sn_{0.99}Te$, to ~ 0.25 eV for $Mn_{0.05}Sn_{0.95}Te$, and to ~ 0.20 eV for $Mn_{0.09}Sn_{0.91}Te$, Figure 3(c).

Temperature is another important factor that can dramatically influence the band structure especially in the group 14 chalcogenides and materials featuring multiple valence bands. Figure 3(d) shows the Pisarenko lines at 300 and 800 K.[10] The data for our Mn alloyed SnTe samples at 800 K exhibits much higher Seebeck coefficients than the calculated ones, compared with those at 300 K, which indicates that rising temperature may be reducing the energy separation between the light- and heavy-hole bands.

Evidence for changes in the valence band structure with Mn fraction and temperature comes from the temperature-dependence of the Hall coefficient, R_H. In rock-salt IV-VI semiconductors which are known for their two-valence-band character, the change of R_H peak can reflect the valence band structure change as a function of temperature and doping level. This phenomenon is especially obvious in the heavily doped systems,[2, 5] where the increased carrier density pushes the Fermi level closer to the maximum of the heavy-hole valence band. As temperature increases, the upper L band lowers its energy to converge with the lower Σ band, as schematically shown in Figure 3(a); an increasing number of holes will be transferred to the low-mobility Σ band and contribute to the Hall effect, resulting in carrier redistribution between the two bands and a strong temperature-dependence nonmonotonic variation of R_H.[35] The analysis of the temperature-dependence of Hall coefficient can been carried out using the following formula:[36]

$$\frac{R(T)-R(0)}{R(0)} = (1-\frac{\mu_2}{\mu_1})^2(\frac{m_2^*}{m_1^*})^{3/2}\exp(-\Delta E_V / k_BT) \qquad (5)$$

where *R(0)* is the Hall coefficient at 0 K, μ_1 (μ_2) and m_1^* (m_2^*) are the carrier mobility and effective mass of high-energy hole band and low-energy hole band respectively. ΔE_V is the energy separation between the two valence bands. Compared with the *L* band, the *Σ* band exhibits lower carrier mobility, but higher effective mass. At certain temperature, when the contribution from two types of carriers with different effective masses and different carrier mobilities to conduction is equal, the R_H peaks. The peak temperature of R_H is strongly dependent on ΔE_V (ΔE_V=0, R_H climbs to the peak). Therefore, the change in R_H peak with Mn fraction reflects the valence band structure modification. Figure 3(e) shows the temperature-dependent Hall coefficients of pure SnTe, 3%- and 9%-Mn alloyed SnTe. It is readily seen that R_H peaks shift to lower temperature from x=0 to x=9%, specifically, 773 K, 624 K, 475 K for pure SnTe, 3%-, 9%-Mn alloyed SnTe, respectively. Since ΔE_v is 0.35 eV at 300 K for SnTe, its valence bands converge at relatively high temperature, about 773 K. MnTe alloying can significant reduce the ΔE_v; and as a result the valence band convergence occurs at a lower temperature, about 475 K. It is worth noting that the R_H peak temperature (~475 K) for $Sn_{1-x}Mn_xTe$ is much lower than that of $Sn_{1-x}Cd_xTe$ (~650 K) and $Sn_{1-x}Hg_xTe$ (~540 K), which reflects the stronger band structure tuning effect by the higher solubility of MnTe.

The Mn-induced valence band convergence and band gap enlargement of SnTe can be further supported by first-principles electronic structure calculations based on density functional theory (DFT). The influence of a 7.4% Mn concentration on the electronic band structures and density of states of SnTe was investigated in detail. As two Sn atoms in the 3×3×3 supercell of SnTe are substituted with Mn atoms, four different atomic configurations are found to be inequivalent; considering the magnetic orderings of the Mn atoms, we obtain eight different band structures for the $Sn_{25}Mn_2Te_{27}$ supercell, as shown in Figure 4. The atomic configurations corresponding to Figure 4(c) and 4(d) are more energetically favorable, while the antiferromagnetic (AFM) ordering always has lower total energies compared to the ferromagnetic (FM) ordering. Nonetheless, we see that Mn increases the band gap and

decreases the energy offset between L and Σ bands in all of the eight configurations investigated. It is seen from the electronic density of states (DOS), as shown in Figure 5, that doping Mn into SnTe does not create resonant states, which are usually characterized by a local DOS hump slightly above the Fermi level.[10] Therefore, the reasons for the enhancement of Seebeck coefficient are not believed to originate in the generate of resonant states[37].

3.4. Thermal transport properties

The total thermal conductivity (κ_{tot}) in the SnTe-x%MnTe system shows a significant decrease with increasing Mn fraction, Figure 6(a). Specifically, at room temperature, the κ_{tot} of SnTe is above ~ 8.0 $Wm^{-1}K^{-1}$, and it is dramatically reduced to less than 2.5 $Wm^{-1}K^{-1}$ at x>17%. κ_{tot} is the sum of the electronic (κ_{ele}) and lattice thermal conductivity (κ_{lat}). κ_{ele} is proportional to the electrical conductivity σ through the Wiedemann-Franz relation, $\kappa_{ele}=L\sigma T$, where L is the Lorenz number. Due to the complexity and the non-parabolicity of the valence band structure around the Fermi level for p-type SnTe, accurate determination of the L is difficult. An estimation of L can be made using a single parabolic band (SPB) model with acoustic phonon scattering, resulting in an L with a deviation of less than 10% as compared with a more rigorous single non-parabolic band and multiple band models calculation.[24] Heat capacity, thermal diffusivity, Lorenz number and electronic thermal conductivity for $Sn_{1-x}Mn_xTe$ are shown in Figure S3.

The κ_{lat} shows a trend of first decreasing and then increasing with x, as shown in Figure 6(b). At room temperature the κ_{lat} continuously decreases from 2.5 $Wm^{-1}K^{-1}$ for x=0 to 1.2 $Wm^{-1}K^{-1}$ for x=17%, and then rises to 1.6 $Wm^{-1}K^{-1}$ for x=20%. Correspondingly, the κ_{lat} at 900 K decreases from 1.6 $Wm^{-1}K^{-1}$ for x=0 to 0.6 $Wm^{-1}K^{-1}$ for x=17%, and then rises to 0.9 $Wm^{-1}K^{-1}$ for x=20%. This reduction in κ_{lat} indicates that MnTe can significantly modify the microstructure of SnTe, as well-dispersed nanostructures and atomic-scale defects can be expected to effectively scatter phonons from short wavelength to long wavelength. The rise in κ_{lat} at heavily Mn alloyed samples hints that the microstructure tuning *via* Mn alloying is complex, because of

layered MnTe second phase with higher thermal conductivity along the layer extension direction, will be discussed later.

As shown in Figure 6(c), with increasing Mn fraction, both κ_{ele} and κ_{lat} are significantly lowered, with the κ_{ele} dropping much faster. At low Mn fractions, the electronic contribution to κ_{tot} is dominant, but κ_{lat} is the major part in the heavily Mn alloyed SnTe (>7%) samples. Specifically, the ratio of $\kappa_{lat}/\kappa_{tot}$ is 30% for SnTe at room temperature and rises to 55.6% for x=9%, and to 63.7% for x=20%, see Figure 6(d).

3.5. Bipolar effect suppression

For samples with x<3% the κ_{tot} of $Sn_{1-x}Mn_xTe$ shows an obvious upturn at higher temperature. When x exceeds 3%, a flattening trend is observed Figure 6(a). The κ_{lat} follows the trend of κ_{tot}, Figure 6(b). The upturns in both κ_{tot} and κ_{lat} at higher temperature are indicative of the bipolar effect in SnTe, as widely observed in V_2-VI_3 and IV-VI (V=Bi, Sb; IV=Ge, Sn, Pb; VI=S, Se, Te) thermoelectric systems.[4, 5, 38-41] This effect is especially pronounced in narrow band gap materials. Minority carriers are thermally excited across the band gap and the diffusing electron–hole pair gives rise to an additional thermal conductivity contribution, i.e. the bipolar thermal conductivity, which raises the total thermal conductivity. These bipolar effects also degrade the Seebeck coefficients, because the thermally minority carriers, have Seebeck coefficient of opposite sign, and offset that of the majority ones. Therefore, bipolar effects limit the *ZT* at higher temperatures. The bipolar effect in SnTe-based thermoelectric materials as reflected in the Seebeck coefficient (Figure 2(b)) is not pronounced as in Pb*Q* and V_2-VI_3 systems,[4, 5, 38-41] because of its very high hole concentration (majority carrier), which is similar with GeTe.[35] To suppress the bipolar effect several strategies have been explored: (1) increasing the majority carrier concentration through heavy doping;[4, 42] (2) enlarging the band gap;[5] (3) building up energy barrier filters through nanostructuring grains.[38,21] In the present work, Mn alloying could concurrently serve the first two approaches. The hole (majority carrier) concentration is increased *via* rising Mn fraction, which pushes the Fermi level E_F

deeper into valence band. This increases the energy distance between the Fermi level and the conduction band, which decreases the probability that electrons are thermally excited into the conduction band, and suppresses the bipolar diffusion.

If the bipolar effect is not taken into account, the lattice thermal conductivity κ_{lat} is always overestimated since the extra term (bipolar thermal conductivity, κ_{bip}) in Eq (6) is ignored[5, 43]:

$$\kappa_{tot} - \kappa_{ele} = \kappa_{lat} + \kappa_{bip}, \qquad (6)$$

In order to clarify the contribution of bipolar thermal conductivity κ_{bip} at high temperature, the κ_{tot}-κ_{ele} and κ_{lat} as a function of temperature need to be identified. If we consider only the predominant acoustic phonon scattering at low temperatures before bipolar diffusion is significant (κ_{bip}= 0), κ_{tot}-κ_{ele} equals to κ_{lat}, and the κ_{lat} can be approximately given as:[5, 43]

$$\kappa_{lat} \propto MV^{1/3}\theta_D^3\gamma^{-2}T^{-1}, \qquad (7)$$

where M is the average mass per atom, V the average atomic volume, θ_D the Debye temperature, and γ the Grüneisen parameter. Note that according to Eq(7), κ_{lat} is linearly proportional to T^1.

The plots of κ_{tot}-κ_{ele} as a function of 1000/T for pure SnTe and 9% Mn alloyed SnTe are shown in Figure 6(e). For SnTe, as the temperature is increased to 523 K, the κ_{tot}-κ_{ele} starts to gradually deviate from a linear relationship between κ_{lat} and T^1 because the bipolar diffusion starts to contribute to the thermal conductivity. The κ_{bip} at high temperatures was estimated by subtracting the extrapolated linear κ_{lat}-T^1 relationship (indicated by the dashed line in Figure 6(e)) from the respective κ_{tot}-κ_{ele}, as shown in the inset of Figure 6(f). However, for the 9% Mn alloyed SnTe sample, no departure from the linear dependence at high temperature can be observed in Figure 6(f). This is attributed to the enlarged band gap and diminished bipolar contribution with increasing Mn alloying fractions in SnTe.

To avoid the deterioration of overall thermoelectric properties by the bipolar effect, the band gap should be larger than the energy jump for bipolar diffusion, E_{bip}. The E_{bip} can be roughly estimated from the following relationship:[5, 44]

$$\kappa_{\text{bip}} \propto A \exp\left(\frac{-E_{bip}}{2k_B T}\right), \qquad (8)$$

where A is a constant. Since the bipolar effect can be obviously suppressed when Mn alloyed fraction is larger than 3%, it suggests the band gap of these samples should be larger than E_{bip} at high temperature (e.g. >700 K).

3.6. **Multiple phonon scattering**

In order to explore the underlying physical mechanisms of the observed low lattice thermal conductivities of Mn alloyed SnTe, we look through the microstructure using analytical (scanning) transmission electron microscopy STEM. Here, the x=19% sample was selected, since it contains more obvious MnTe laminates than the x=17% sample, and higher density of nanoprecipitates than the x=9% sample, as discussed below.

The medium-magnification TEM and Bright-field STEM image in Figures 5(a) and (b) respectively, show high density of nanoscale precipitates. The peculiar feature here is the portion of nanoprecipitates with Ashby-Brown contrast. Ashby-Brown contrast is one of the strain contrasts used to image coherent spherical particles.[45, 46] Under the two-beam condition in bright field or bright-field STEM with high strain-field sensitivity (Figure 7(b)), a coherent precipitate is represented by two half-moon shaped regions of contrast with a no-contrast line perpendicular to the **g** vector. The no-contrast line corresponds to the plane without distortion. When the interface coherency evolves, the spherical strain contrast will change its symmetry and the fringes will appear. Another portion of nanoprecipitates are without Ashby-Brown contrast, but the interface between the precipitates and the matrix is also coherent, as shown in Figure 7(c). These nanoprecipitates with endotaxial relationship with the matrix can scatter heat-carrying phonons effectively, but not greatly scatter carriers, allowing a higher figure of merit to develop.

Besides the nanoscale precipitates, MnTe laminates are also found when the Mn fraction is larger than 15%. Figure S4 is a TEM image showing several laminates in SnTe. Because of strong strain-field effect observed in TEM mode, it is difficult to

observe the contrast difference between the lamellar second phases and the matrix. In contrast, the high angle annular dark field (HAADF) STEM mode can clearly show such differences due to the Z-contrast features. As shown in Figure 8(a), the laminates (50-200 nm in width, while several μm in length) exhibit slightly weaker contrast than the matrix, hinting the laminates are Mn-rich. Furthermore, the matrix presents high density of "messy" strain-field contrast due to defects and nanoprecipitates (as discussed in Figure 7), while the laminates exhibit clear contrast.

X-ray energy dispersive spectroscopy (EDS) in STEM mode using a nanometer probe was employed to confirm the composition of the two phases. The compositional line scan across a laminate (green line marked in Figure 8(a)) is plotted in Figure 8(b). The relative counts of Mn are much higher in the laminate than in the matrix, while the reverse is true for Sn. More accurate determination of composition was done with EDS point analysis. EDS spectra in Figure 8(c) were obtained from an laminate and its adjacent matrix: peaks for Te are equal in both laminate and the matrix; peaks for Mn and Sn exclusively exist as the main peaks for the laminate and the matrix; meanwhile, they present as minor peaks for the other one. This indicates that both the laminate and the matrix are not pure MnTe and SnTe, but with certain solid solution of Sn and Mn, respectively. A semi-quantitative composition analysis of EDS point spectrum is shown in Figure 8(d). This is a statistical plot from many sets of points taken from MnTe laminates and SnTe matrix. The composition of MnTe laminates and SnTe matrix was estimated as $Mn_{3.6}Sn_{44.6}Te_{51.8}$ and $Mn_{48.4}Sn_{3.1}Te_{48.5}$, respectively.

Figure 9(a) is a medium-magnification TEM image showing one MnTe laminate inserted in the SnTe matrix. The electron diffraction pattern shown in Figure 9(b) was obtained with a small selective aperture including the two different regions of contrast showing the superposition of MnTe and SnTe. Then high-resolution transmission electron microscopy (HRTEM) was adopted to study the detailed microstructural features of the above MnTe laminate and SnTe matrix, as shown in Figure 9(c-e). The fast Fourier transformation (FFT) image (inset in Figure 9(c)) exhibits an alignment of MnTe laminate and SnTe matrix without too large Bragg reflection splitting. The

enlarged lattice image of the interface can more clearly show the crystallographic relation between the MnTe laminate and the SnTe matrix, i.e., $[-121]_{SnTe}$// $[001]_{MnTe}$. The inverse FFT (IFFT) image of Figure 9(d) presents an array of edge dislocations, which is quite similar to the case of PbTe-PbS phase boundary, studied previously.[4, 47] Although the structure of MnTe (hexagonal) is different from the structure of SnTe (cubic), it still tends to grow along certain planes with minimum lattice mismatch. Such semi-coherent interface with misfit dislocations separated by elastic strain can contribute much to phonon scattering with medium and long wavelengths, meanwhile maintaining good carrier transport without excessive scattering.[4, 47]

Interestingly, there are more delicate structural features inside the MnTe laminates. The HRTEM image in Figure 10(a) exhibits a whole image of a MnTe laminate: the MnTe layers are interrupted by several anomalous "lines", which are reflected as diffuse spots along the [001] directions occurring between the main MnTe reflection spots. To observe these features more clearly, two "lines" are focused in Figure 9(c). Actually, the "lines" at relatively low magnification embrace 10-layers of lattice which disturb the pure 4-layer lattice of MnTe matrix, i.e., stacking faults. In crystallography, a stacking fault is a type of planar defect which derives from disordering of crystallographic planes, especially for layered structures. Figure 10(d) and 10(e) show enlarged lattice images from Figure 10(c), separately showing the MnTe matrix and a stacking fault. Inversely, pure MnTe superlattices without any diffuse spots can be found in the SnTe matrix, Figure 10(f), while diffuse spots are clearly present between the main reflection spots.

As described above, SnTe samples heavily alloyed with MnTe exhibit multiple types of microstructural features as follows: (1) SnTe matrix with nanoscale precipitates, as shown in Figure 7; (2) MnTe second phase in SnTe matrix as laminates, Figure 8, and respective interfaces between MnTe laminates and SnTe matrix, Figure 9; (3) stacking faults inside MnTe laminates, Figure 10; (4) 4-layer MnTe main lattice and 10-layer lattice inside the stacking faults, Figure 10; (5) point defects due to solid solution and respective strains on the atomic scale. These microstructural features along with the mesoscale grains in these samples define a

multi-scale hierarchical architecture that can scatter phonons of a broad range of different wavelengths and mean free paths. Although MnTe laminates play an important role in phonon scattering, it does not mean the more laminates are present the better. If these MnTe laminates grow too large-scale, i.e., its width approaches the micrometer scale, then the thermal transport properties of the MnTe phase will come into play raising the total thermal conductivity.[48] This is likely the reason why the thermal conductivity rises when the MnTe fraction is above 17%. On the other hand, when the MnTe fraction is between the solid solution and the value when large-scale MnTe phase forms, e.g., x=9%, the microstructure becomes similar to those in PbTe-based systems,[3-5] where high density of nanoprecipitates and point defects contribute dominantly to the phonon scattering.

3.7. Concluding remarks

As we have shown above the *ZT* value of SnTe is systematically increased upon MnTe alloying with peak *ZT* at 900 K. Compared to pure SnTe, *ZT* is enhanced from 0.6 to 1.2 for x=9% Mn-alloyed SnTe and further to 1.3 for the x=17% sample, Figure 11(a). As the Mn fraction increases, the overall thermoelectric performance experiences two peaks at x=9% and 17%, which reflects the trend of the Seebeck coefficient and thermal conductivity. Mn alloying modifies significantly the valence band structure of SnTe, which results in an enhancement of the Seebeck coefficient. Figure 11(b) compares the temperature-dependent *ZT* values of other reported SnTe systems.[2,10]

The substitution of Sn with Mn atoms in SnTe leads to a series of profound effects: (a) it pushes down the Fermi level deep into the valence band by increasing the hole concentration, suppressing the bipolar effect, and enhancing the Seebeck coefficient at elevated temperature; (b) it creates a strong valence band structure modification than other dopants, e.g. Cd, Hg, In and Mg because of its higher solubility. This brings the two valence bands closer in energy and contributes to enhancement of the Seebeck coefficient; (c) at higher fractions x>9% MnTe induces nanoscale precipitates, laminates, stacking faults and layers, which effectively scatter phonons on multiple

length scales, leading to very low lattice thermal conductivities. It is encouraging that Mn alloying brings out the high performance of SnTe, suggesting that further improvements are possible with a deeper understanding of alloying processes in SnTe. The present system exhibits one of the highest average *ZT* values of ~0.5 (from 300 K to 900 K), which is important in determining device efficiency, Figure 11(c). The high performance could make SnTe as a serious candidate for consideration in medium temperature thermoelectric power generation.

Acknowledgement

This work was supported as part of the Revolutionary Materials for Solid State Energy Conversion, an Energy Frontier Research Center funded by the U.S. Department of Energy, Office of Science, and Office of Basic Energy Sciences under Award Number DE-SC0001054; This work was also supported by the "Zhuoyue" program of Beihang University, the Recruitment Program for Young Professionals, and NSFC under Grant No. 51571007 (L.D.Z); This is also partly supported by the startup fund from South University of Science and Technology of China from Shenzhen government and national 1000 plan for young scientists (J.Q.H); and partly supported by NSFC under Grant No. 51202008 and Postdoctoral Science Foundation of China (2013M540037) (Y.L.P); Transmission electron microscopy work was performed in Center of Electron Microscopy in Zhejiang University, Hangzhou, China (H.J.W).

Reference

1. L. D. Zhao, V. P. Dravid and M. G. Kanatzidis, *Energy & Environmental Science*, 2014, **7**, 251-268.
2. Y. Pei, X. Shi, A. LaLonde, H. Wang, L. Chen and G. J. Snyder, *Nature*, 2011, **473**, 66-69.
3. K. Biswas, J. He, I. D. Blum, C.-I. Wu, T. P. Hogan, D. N. Seidman, V. P. Dravid and M. G. Kanatzidis, *Nature*, 2012, **489**, 414-418.
4. H. J. Wu, L. D. Zhao, F. S. Zheng, D. Wu, Y. L. Pei, X. Tong, M. G. Kanatzidis and J. Q. He, *Nat Commun*, 2014, **5**.
5. L. D. Zhao, H. J. Wu, S. Q. Hao, C. I. Wu, X. Y. Zhou, K. Biswas, J. Q. He, T. P. Hogan, C. Uher, C. Wolverton, V. P. Dravid and M. G. Kanatzidis, *Energy & Environmental Science*, 2013, **6**, 3346-3355.

6. X. Zhang and L.-D. Zhao, *Journal of Materiomics*, 2015, **1**, 92-105.
7. L. D. Zhao, S. H. Lo, Y. S. Zhang, H. Sun, G. J. Tan, C. Uher, C. Wolverton, V. P. Dravid and M. G. Kanatzidis, *Nature*, 2014, **508**, 373-+.
8. P. B. Littlewood, *Journal of Physics C: Solid State Physics*, 1980, **13**, 4855.
9. S. Santhanam and A. K. Chaudhuri, *Materials Research Bulletin*, 1981, **16**, 911-917.
10. Q. Zhang, B. Liao, Y. Lan, K. Lukas, W. Liu, K. Esfarjani, C. Opeil, D. Broido, G. Chen and Z. Ren, *Proceedings of the National Academy of Sciences*, 2013, **110**, 13261-13266.
11. G. Tan, L.-D. Zhao, F. Shi, J. W. Doak, S.-H. Lo, H. Sun, C. Wolverton, V. P. Dravid, C. Uher and M. G. Kanatzidis, *Journal of the American Chemical Society*, 2014, **136**, 7006-7017.
12. G. Tan, F. Shi, H. Sun, L.-D. Zhao, C. Uher, V. P. Dravid and M. G. Kanatzidis, *Journal of Materials Chemistry A*, 2014, **2**, 20849-20854.
13. G. Tan, F. Shi, S. Hao, H. Chi, L.-D. Zhao, C. Uher, C. Wolverton, V. P. Dravid and M. G. Kanatzidis, *Journal of the American Chemical Society*, 2015, **137**, 5100-5112.
14. G. Tan, F. Shi, J. W. Doak, H. Sun, L.-D. Zhao, P. Wang, C. Uher, C. Wolverton, V. P. Dravid and M. G. Kanatzidis, *Energy & Environmental Science*, 2015, **8**, 267-277.
15. A. Banik, U. S. Shenoy, S. Anand, U. V. Waghmare and K. Biswas, *Chemistry of Materials*, 2015, **27**, 581-587.
16. A. J. Minnich, M. S. Dresselhaus, Z. F. Ren and G. Chen, *Energy & Environmental Science*, 2009, **2**, 466-479.
17. M. Zebarjadi, K. Esfarjani, M. S. Dresselhaus, Z. F. Ren and G. Chen, *Energy & Environmental Science*, 2012, **5**, 5147-5162.
18. J.-F. Li, W.-S. Liu, L.-D. Zhao and M. Zhou, *Npg Asia Materials*, 2010, **2**, 152-158.
19. G. J. Snyder and E. S. Toberer, *Nature Materials*, 2008, **7**, 105-114.
20. L.-D. Zhao, J. He, D. Berardan, Y. Lin, J.-F. Li, C.-W. Nan and N. Dragoe, *Energy & Environmental Science*, 2014, **7**, 2900-2924.
21. Y. Pei, A. D. LaLonde, N. A. Heinz, X. Shi, S. Iwanaga, H. Wang, L. Chen and G. J. Snyder, *Advanced Materials*, 2011, **23**, 5674-5678.
22. H. Wang, Y. Pei, A. D. LaLonde and G. J. Snyder, *Advanced Materials*, 2011, **23**, 1366-1370.
23. G. Tan, F. Shi, S. Hao, H. Chi, T. P. Bailey, L.-D. Zhao, C. Uher, C. Wolverton, V. P. Dravid and M. G. Kanatzidis, *Journal of the American Chemical Society*, 2015, DOI: 10.1021/jacs.1025b07284.
24. L.-D. Zhao, S.-H. Lo, J. He, H. Li, K. Biswas, J. Androulakis, C.-I. Wu, T. P. Hogan, D.-Y. Chung, V. P. Dravid and M. G. Kanatzidis, *Journal of the American Chemical Society*, 2011, **133**, 20476-20487.
25. J. P. Perdew, K. Burke and M. Ernzerhof, *Physical Review Letters*, 1996, **77**, 3865-3868.
26. G. Kresse and D. Joubert, *Physical Review B*, 1999, **59**, 1758-1775.
27. G. Kresse and J. Furthmüller, *Physical Review B*, 1996, **54**, 11169-11186.
28. H. J. Monkhorst and J. D. Pack, *Physical Review B*, 1976, **13**, 5188-5192.
29. J. Q. Li, Z. W. Lu, H. J. Wu, H. T. Li, F. S. Liu, W. Q. Ao, J. Luo and J. Q. He, *Acta Materialia*, 2014, **74**, 215-223.
30. J. P. Heremans, V. Jovovic, E. S. Toberer, A. Saramat, K. Kurosaki, A. Charoenphakdee, S. Yamanaka and G. J. Snyder, *Science*, 2008, **321**, 554-557.
31. H. J. Goldsmid, *Applications of Thermoelectricity* Butler & Tanner Ltd., London, 1960.
32. R. F. Brebrick and A. J. Strauss, *Physical Review*, 1963, **131**, 104-110.
33. W.-S. Liu, Q. Zhang, Y. Lan, S. Chen, X. Yan, Q. Zhang, H. Wang, D. Wang, G. Chen and Z. Ren,

Advanced Energy Materials, 2011, **1**, 577-587.

34. Q. Zhang, B. Liao, Y. Lan, K. Lukas, W. Liu, K. Esfarjani, C. Opeil, D. Broido, G. Chen and Z. Ren, *Proceedings of the National Academy of Sciences of the United States of America*, 2013, **110**, 13261-13266.
35. D. Wu, L.-D. Zhao, S. Hao, Q. Jiang, F. Zheng, J. W. Doak, H. Wu, H. Chi, Y. Gelbstein, C. Uher, C. Wolverton, M. Kanatzidis and J. He, *Journal of the American Chemical Society*, 2014, **136**, 11412-11419.
36. I. U. r. I. Ravich, B. A. e. Efimova and I. A. Smirnov, *Semiconducting lead chalcogenides*, Plenum Publishing Corporation, 1970.
37. J. P. Heremans, B. Wiendlocha and A. M. Chamoire, *Energy & Environmental Science*, 2012, **5**, 5510-5530.
38. H. Wu, J. Carrete, Z. Zhang, Y. Qu, X. Shen, Z. Wang, L.-D. Zhao and J. He, *NPG Asia Mater*, 2014, **6**, e108.
39. Y.-L. Pei, H. Wu, D. Wu, F. Zheng and J. He, *Journal of the American Chemical Society*, 2014, **136**, 13902-13908.
40. L. Hu, T. Zhu, X. Liu and X. Zhao, *Advanced Functional Materials*, 2014, **24**, 5211-5218.
41. L. Hu, H. Wu, T. Zhu, C. Fu, J. He, P. Ying and X. Zhao, *Advanced Energy Materials*, 2015, n/a-n/a.
42. H. J. Goldsmid, *Proceedings of the Physical Society*, 1958, **71**, 633.
43. G. S. Nolas and H. J. Goldsmid, *ed. Tritt, T. M. , in Thermal Conductivity-2003: Theory, Properties and Applications, ed. T. M. Tritt, Kluwer Academic, New York, ,* 2004, 105–121.
44. O. C. Yelgel and G. P. Srivastava, *Phys. Rev. E: Stat., Nonlinear, Soft. Matter Phys.*, 2012, **85**, 12.
45. W. Chihiro, W. Daizen and M. Ryoichi, *Mater Trans*, 2006, **47**, 2285-2291.
46. S. Iwamura and Y. Miura, *Acta Materialia*, 2004, **52**, 591-600.
47. J. He, S. N. Girard, M. G. Kanatzidis and V. P. Dravid, *Advanced Functional Materials*, 2010, **20**, 764-772.
48. W. Xie, S. Populoh, K. Gałązka, X. Xiao, L. Sagarna, Y. Liu, M. Trottmann, J. He and A. Weidenkaff, *Journal of Applied Physics*, 2014, **115**, 103707.

Figures caption

Figure 1. Solid solution limit of MnTe in SnTe: (a) powder XRD patterns for samples of $Sn_{1-x}Mn_xTe$ (x=0-50%); (b) an enlarged view of (200) Bragg peaks; (c) room temperature lattice parameter as a function of Mn fraction; (d) Rietveld refinement results for the XRD pattern of $Sn_{0.8}Mn_{0.2}Te$.

Figure 2. **Electrical transport properties:** (a) electrical conductivity, (b) Seebeck coefficient, and (e) power factors for $Sn_{1-x}Mn_xTe$; (c) Temperature dependent Seebeck coefficient of pure SnTe, In-,[10] Cd-,[11] Mg-,[15] Mn-, Bi/Hg-,[14] In/Cd-[13] and Ag/Bi-doped[12] SnTe. (d) Seebeck coefficients of SnTe with different dopants at 773 K and 900 K, among which Mn-doped SnTe clearly shows the highest value, especially at high temperature.

Figure 3. Band structure engineering: (a) schematic band structures vary with MnTe fraction and temperature; (b) room temperature Seebeck coefficients for $Sn_{1-x}Mn_xTe$, as well as other SnTe systems, the solid Pisarenko line is calculated based on a two-valence-band model of SnTe; (c) Pisarenko lines are calculated based on a two-valence-band model, considering valence band convergence via Mn alloying. The experimental S vs. N_p values are inserted. (d) Pisarenko lines (300 K and 800 K) compared with experimental Seebeck coefficients, the Seebeck coefficient enhancements suggest the contribution of second valence band especially at elevated temperatures; (e) temperature dependence Hall coefficients for $Sn_{1-x}Mn_xTe$ (x=0, 3%, 9%).

Figure 4. **Electronic band structures of four inequivalent atomic configurations of the $Sn_{25}Mn_2Te_{27}$ supercell computed from DFT:** The distance between the Mn atoms increases from (a) to (d). For each supercell configuration, both ferromagnetic and antiferromagnetic states are considered; the band structure of pristine SnTe is also shown for comparison.

Figure 5. **Density of states of four inequivalent atomic configurations of the $Sn_{25}Mn_2Te_{27}$ supercell computed from DFT:** The distance between the Mn atoms increases from (a) to (d). The vertical line denotes the Fermi level.

Figure 6. **Thermal transport properties and bipolar effect suppression:** (a) temperature dependent total thermal conductivity; (b) temperature dependent lattice thermal conductivity; (c) room temperature total, electronic and lattice thermal conductivities vs. MnTe fraction; (d) the ratio of $\kappa_{lat}/\kappa_{tot}$ as function of MnTe fractions; (e) the (κ_{tot}-κ_{ele}) as a function of 1000/T for pure SnTe and $Sn_{0.91}Mn_{0.09}Te$, the dashed line is linearly fitting to the (κ_{tot}-κ_{ele}) from 300-900 K, deviation of thermal conductivity indicates a significant κ_{bip}; (f) the κ_{bip} as a function of temperature.

Figure 7. **Microstructure of nanoscale precipitates:** both (a) medium-magnification of TEM and (b) bright-field STEM image show high density of nanoscale precipitates; (c) HRTEM image of spherical nanoprecipitates having coherent interface with the matrix.

Figure 8. **Microstructure and chemical identification of MnTe laminates for x=0.19 sample:** (a) STEM HAADF image shows the lamellar MnTe inserted in SnTe matrix; (b) EDS line scanning across the laminate (marked with green line in (a)), shows the laminate is MnTe; (c) EDS point spectra of the MnTe and SnTe regions; (d) statistic plot from many sets of points for MnTe laminates (the above) and SnTe matrix (the below), the composition of MnTe laminates and SnTe matrix can be identified as $Mn_{3.6}Sn_{44.6}Te_{51.8}$ and $Mn_{48.4}Sn_{3.1}Te_{48.5}$, respectively.

Figure 9. Microstructure of phase boundary between MnTe laminate and SnTe matrix for x=0.19 sample: (a) medium-magnification TEM image showing one MnTe laminate inserted into SnTe matrix; (b) electron diffraction pattern with the aperture including the two different regions of contrast showing the superposition of MnTe and SnTe, the SnTe matrix is along [120] zone axis; (c) HRTEM image for SnTe-MnTe phase boundary, the inset is the FFT image; (d) enlarged lattice image for the phase boundary clearly showing the crystallographic relation between MnTe laminate and SnTe matrix; (e) IFFT image showing arrayed dislocations along the interface.

Figure 10. **Layered structure inside the MnTe laminates for x=0.19 sample:** (a) HRTEM image of MnTe laminates showing hierarchical layered structure; (b) FFT image showing diffuse spots along [001] between the main reflection spots; (c) lattice

image showing MnTe 4-layer lattice and two interfaces with 10-layer lattice; (d) enlarged lattice image for the matrix; (e) enlarged lattice image of the interface; (f) FFT image of (d) showing pure MnTe reflections without diffuse spots; (g) FFT image of (e) showing diffuse spots besides the main reflection spots.

Figure 11. ***ZT* and average *ZT*:** (a) temperature dependent *ZT* values for $Sn_{1-x}Mn_xTe$; (b) a comparison of *ZT* values for several SnTe systems, among which SnTe-MnTe clearly has the higher performance; (c) the average *ZT* comparisons with the temperature gradient of 300-900 K.

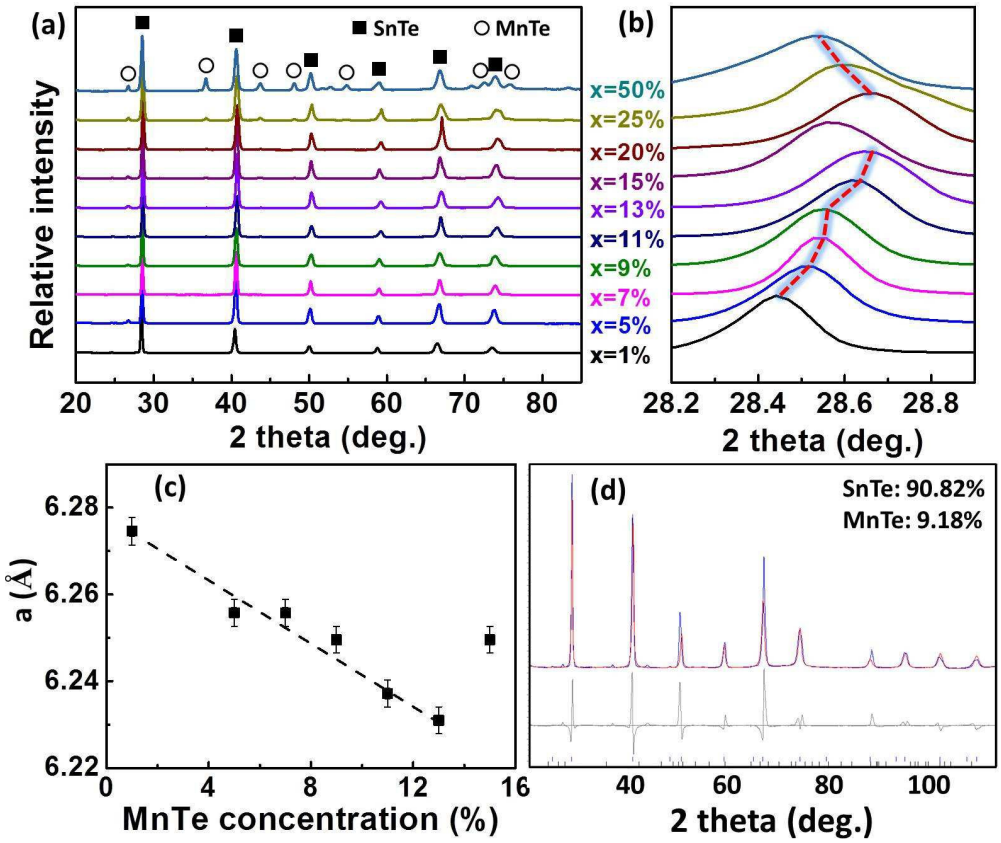

Figure 1

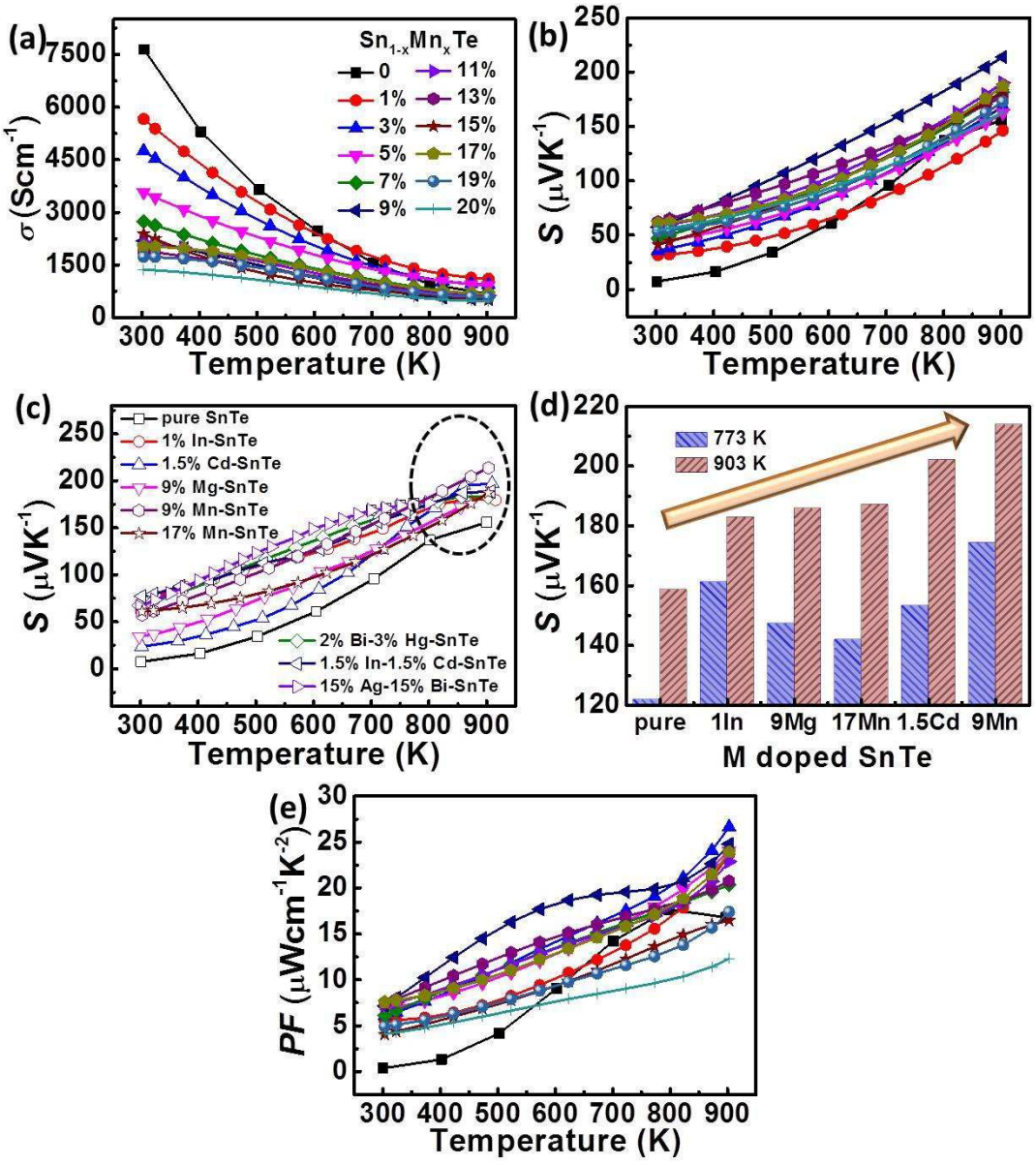

Figure 2

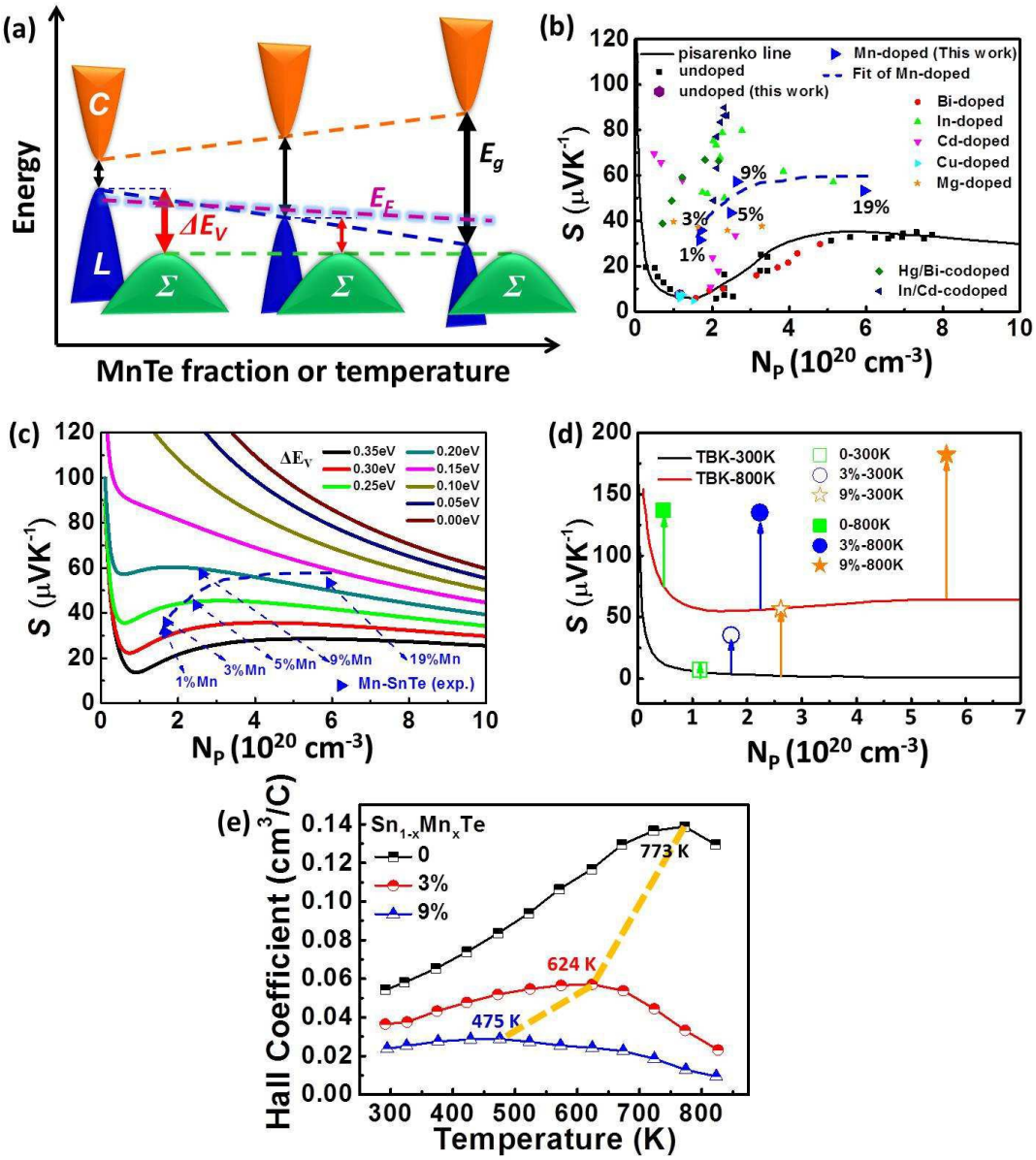

Figure 3

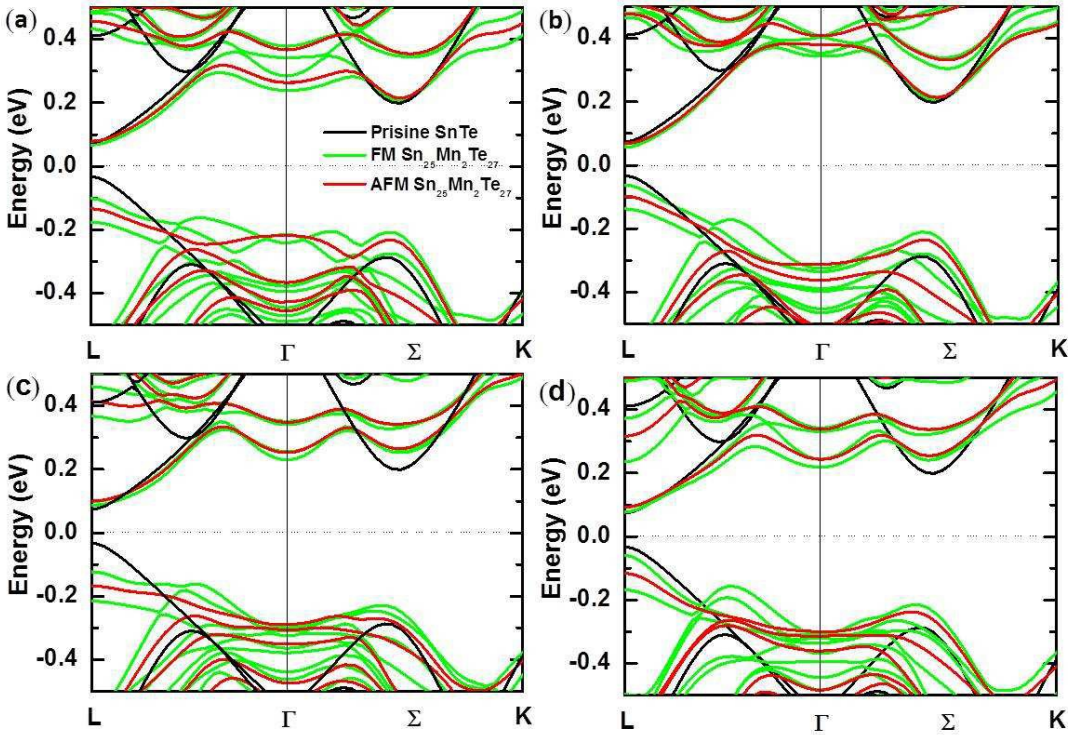

Figure 4

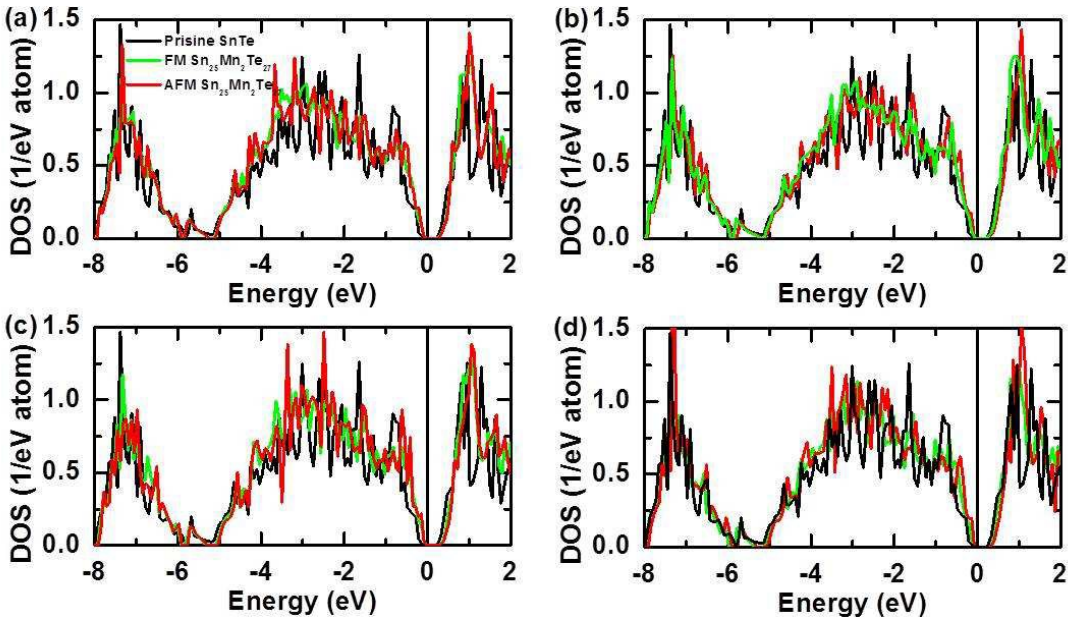

Figure 5

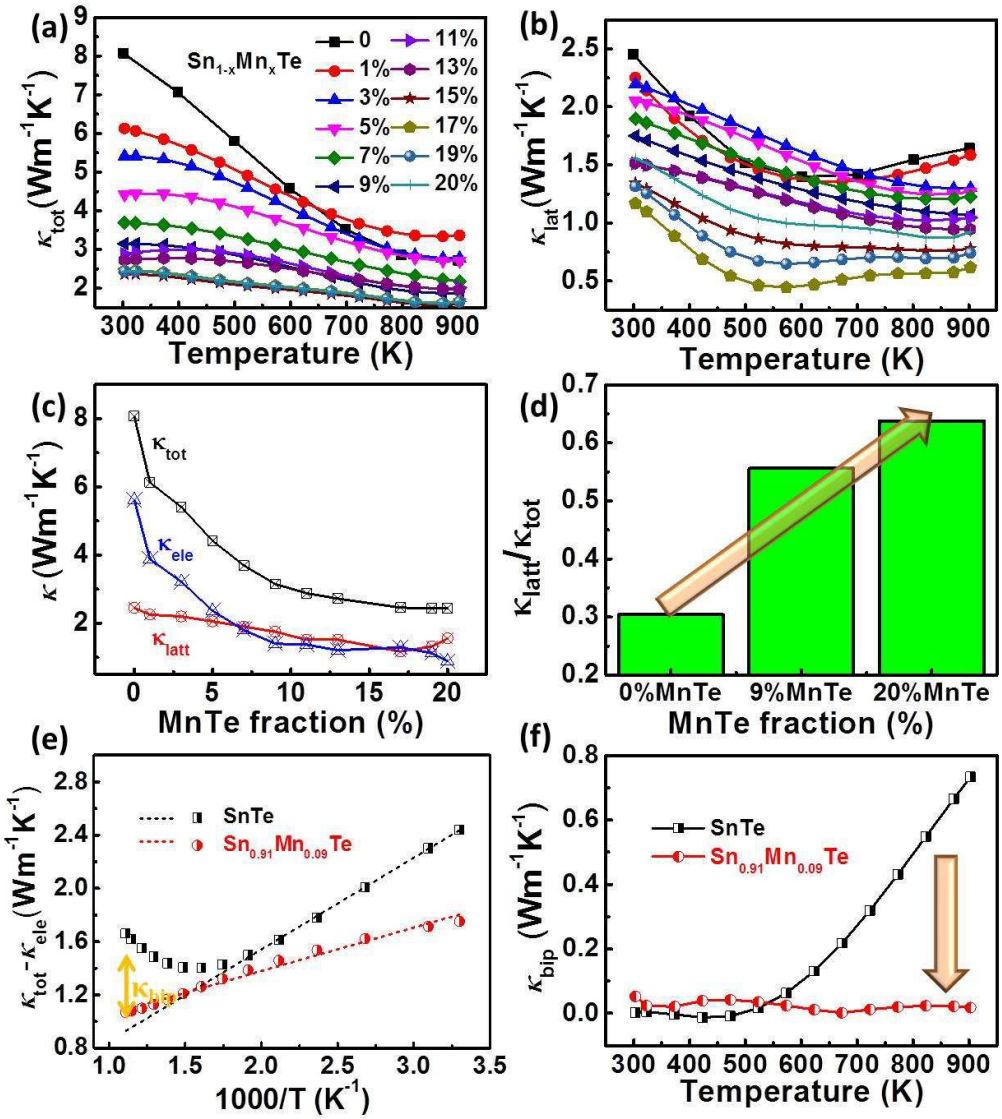

Figure 6

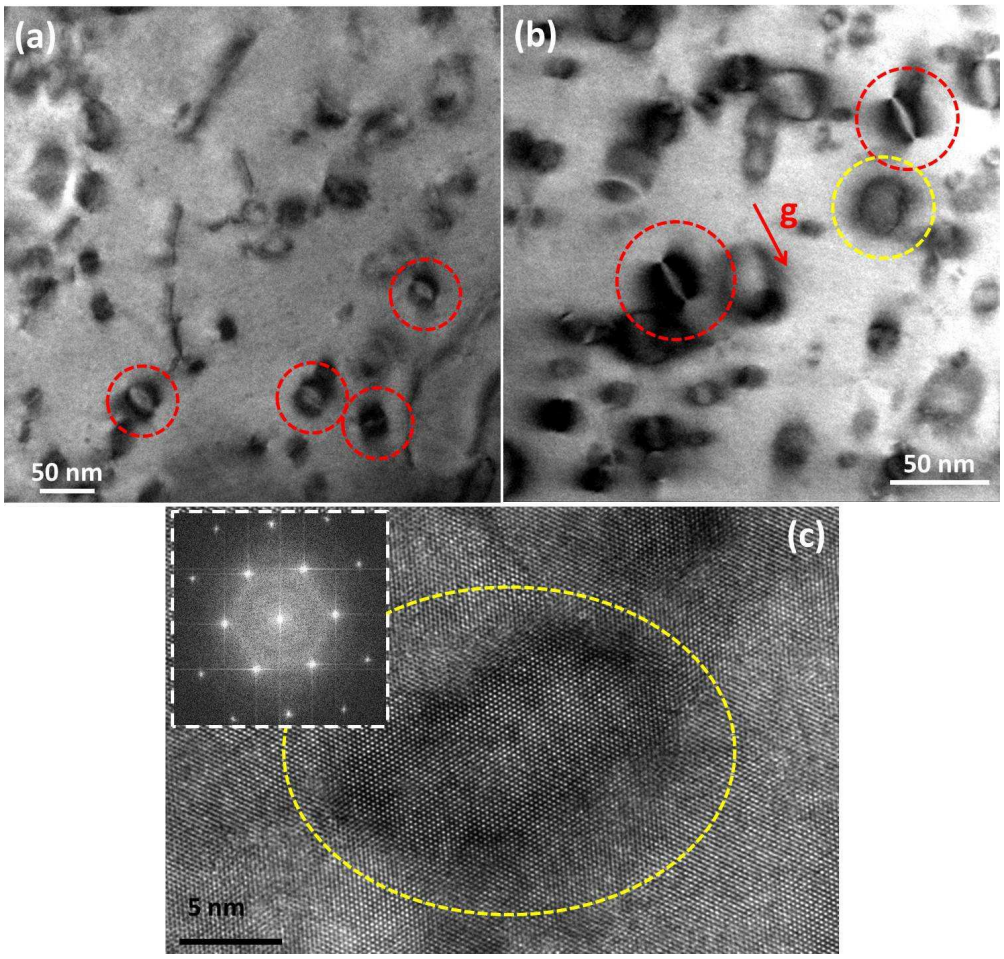

Figure 7

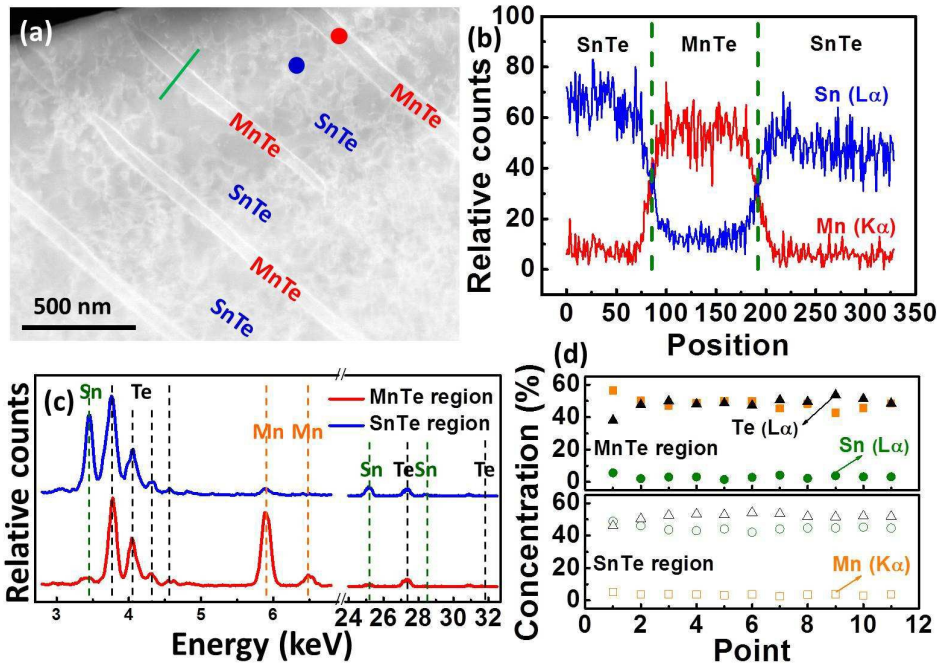

Figure 8

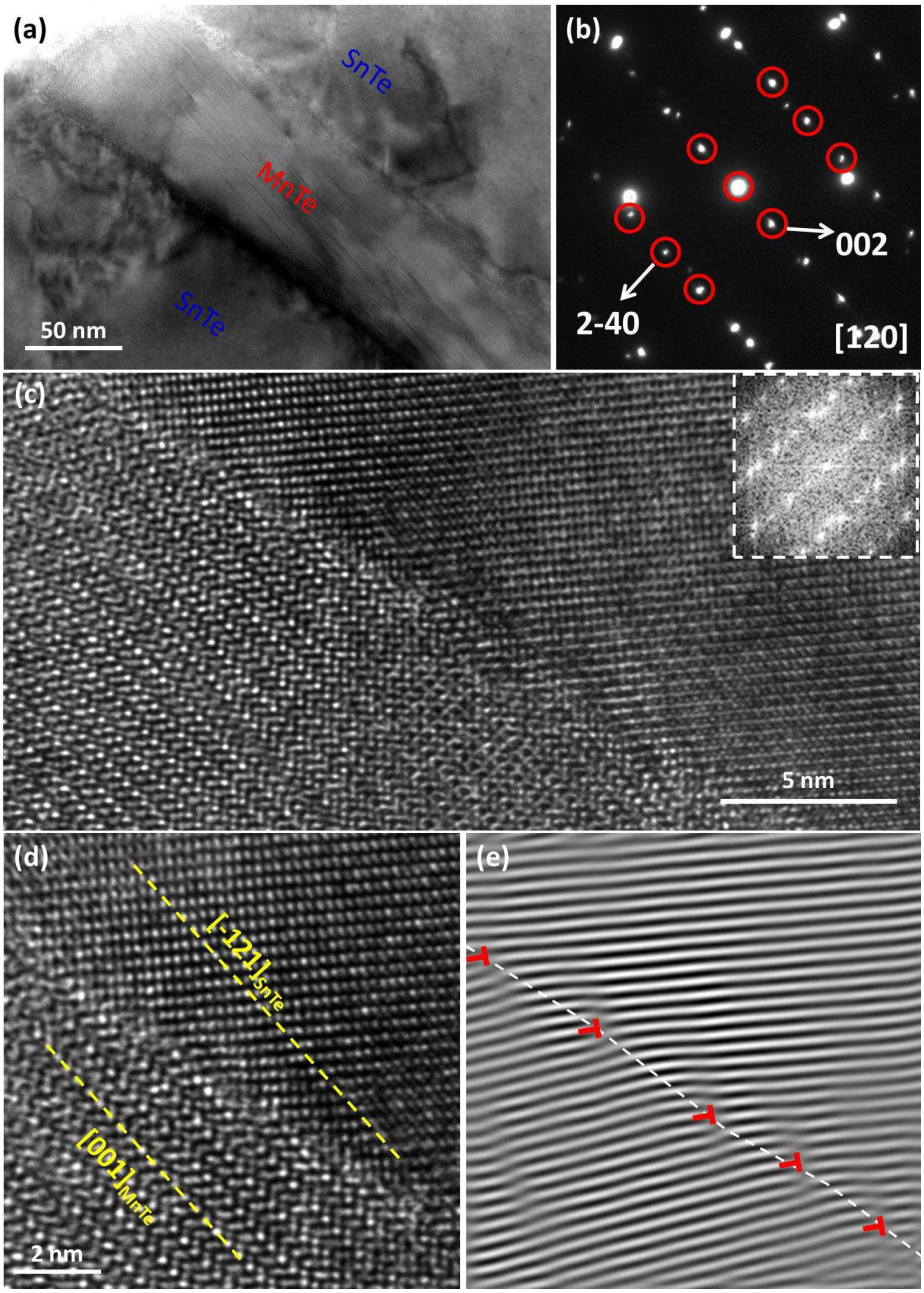

Figure 9

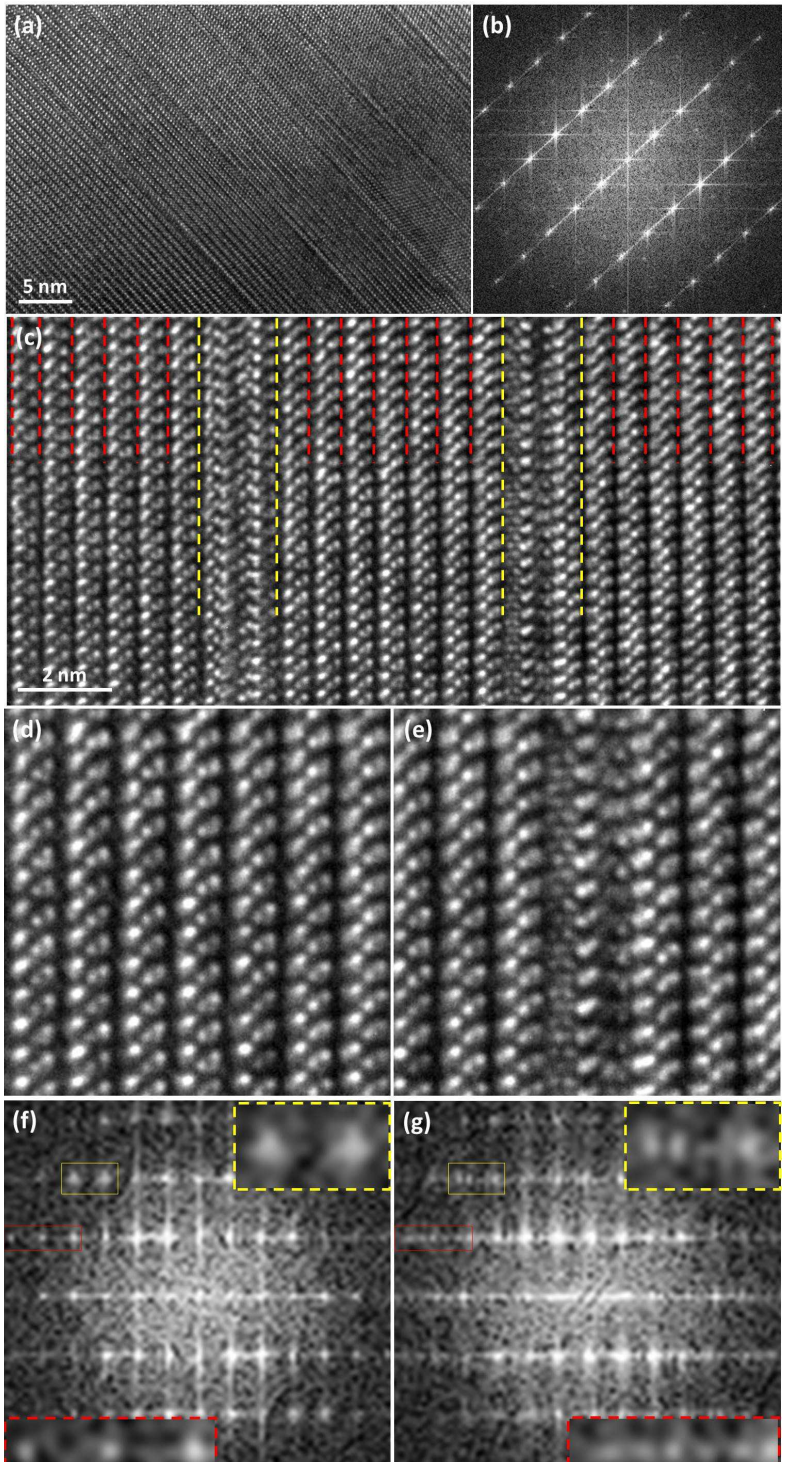

Figure 10

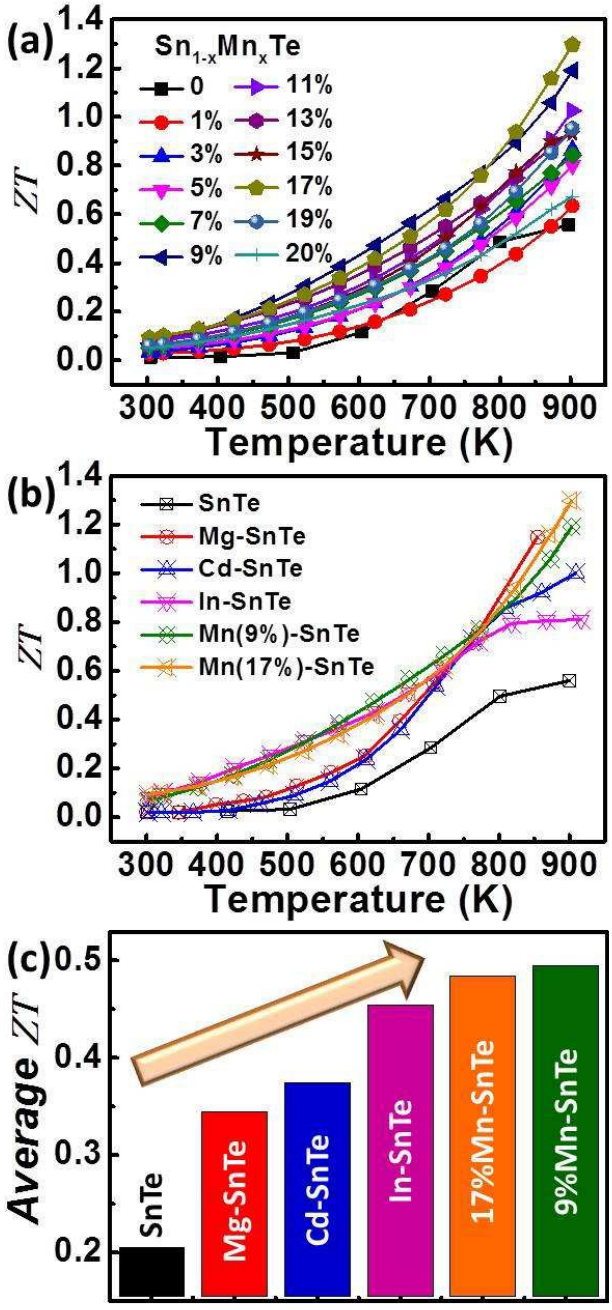

Figure 11

Graphic figure

Heavily MnTe allying can significantly improve the electrical and thermal transport properties of SnTe *via* band structure modifying, multiple phonon scattering and bipolar thermal conductivity suppressing.